Semi-Lagrangian numerical simulation method for tides in coastal regions

Authors

Yoshiki Nishi*, Eiki Taniguchi, Lisa Niikura, and Eitetsu Shibata

* Corresponding author

Department of Systems Design for Ocean-Space, Faculty of Engineering,

Yokohama National University

79-5 Tokiwadai, Hodogaya, Yokohama, Kanagawa 2408501, JAPAN

Tel.: +81 45 339 4087, Fax: +81 45 339 4099

E-mail address: nishi-yoshiki-rg@ynu.ac.jp

Abstract

In this paper, a numerical computation method is proposed to simulate tides in coastal regions. The proposed method is based on the hyperbolic form of governing equations and employs a semi-Lagrangian scheme to ensure the accuracy and stability of numerical computations. Open and wall boundary conditions can be treated universally by combining them with the semi-Lagrangian scheme. Furthermore, the method is applied to some benchmark problems of shallow water to examine its performances in wave propagation, wave transparency through open boundaries, and tides in semi-enclosed bays. The results obtained demonstrate that the proposed method can be utilized as a practical tool to investigate tidal dynamics in coastal regions.

Keywords: tides; semi-Lagrangian; open boundary condition; wall boundary condition; coastal region

Introduction

Computer simulation of tides and tidal currents in coastal seas is a research topic of great interest due to its critical role in predicting the fate of pollutants in seawater and evaluating the potential power of an ocean current. Several numerical computation codes have been constructed to numerically simulate the tides, tidal current, and thermohaline fields. For example, the Princeton Ocean Model (POM) [1] and finite-volume, primitive equation Community Ocean Model (FVCOM) [2] have been widely used by several researchers of physical oceanography and coastal ocean environment because of their ease of usage and excellent performances in theoretical investigations.

However, the numerical ocean model needs to eventually become a practical tool that could be employed in environmental impact assessment against ocean-space utilization and evaluation of environmental risk due to marine pollutants. Therefore, there is a need for continuous efforts to refine the model in order to realize more stable, accurate, and efficient computations. This study aims to provide a fundamental approach to improve numerical ocean model practicality by implementing a new scheme and algorithm.

When predicting the fate of marine pollutants using the ocean model, the tide is one of the most critical factors among a variety of phenomena occurring in the coastal sea; therefore, this study focuses on it primarily. Ocean models developed by earlier studies on tidal simulation can be roughly categorized into the following three groups. The first group refers to models that handle only the external mode of the equations governing the ocean dynamics; whereas the second group includes models that treat the external and internal modes separately and consider the interaction between the two modes as well. The third group is comprised of models that handle the primitive form of the governing equations, which involve the two modes. The model developed in this study falls in the first group since the tidal dynamics addressed by this study can be described as the external mode.

The tidal dynamics can be regarded as the propagation of shallow water wave (long wave). Through mathematical manipulations, the primitive form of the shallow water equation can be transformed into a set of hyperbolic partial differential equations, that is, wave equations. The fact that the performance of the simulation of the external mode depends considerably on the property of numerical computation schemes utilized in solving these hyperbolic-type equations motivated computational fluid dynamics researchers to accurately and stably solve this type of equations. For example, the weighted essentially non-oscillatory (WENO) scheme [3] and constraint interpolation profile (CIP) scheme [4] have been utilized to simulate shallow water successfully. Nonetheless, these schemes have been rarely applied to numerical ocean models.

Accurate solving of the hyperbolic form favors the use of the semi-Lagrangian scheme rather than the Eulerian scheme. When applying the latter scheme, which was employed by most of the existing ocean models, modelers often suffer from unphysical outputs arising from the property of the scheme, thus are required to tune parameters used in the algorithms for providing a balance between the numerical stability and accuracy. The property of the semi-Lagrangian scheme has been improved by the refinement of the method for interpolating values at neighboring two discrete points (e.g., [4]). When the semi-Lagrangian scheme is applied for solving a hyperbolic-type equation, it searches for the solution on a characteristic curve drawn on the spatial-temporal space. This aspect advantages the semi-Lagrangian scheme over the Eulerian one which requires one to implement separately spatial and temporal schemes.

Numerical simulations of coastal ocean dynamics, in general, clips only a part of the area in the ocean within which numerical computations are performed. This treatment requires the boundaries, which do not actually exist, to permit smooth propagation of waves without reflections. Several methods have been proposed to satisfy this boundary condition, which we refer to as open boundary condition.

Most of the previous methods for satisfying this condition are based on the Sommerfeld radiation condition expressed by wave equations. There are varieties of methods for specifying the phase speed included in the equations [5-7]. The theoretical integrity of these methods is however, insufficient, because the governing equations of ocean dynamics involve multiple modes of the waves, thus it is impossible to represent all these waves by a single phase speed. On the other hand, the method proposed by this study has a consistency with the governing equations, because the wave equations used in this study are derived from the governing equation itself, and because they are combined with a fundamental physical law of the wave reflection at an end where the open boundary condition is satisfied.

In the simulation of coastal sea, the condition on the boundary between the land and water, i.e., wall boundary condition, has to be satisfied—the component of flow normal to the wall is inhibited. In previous studies, this condition was satisfied by setting that component to zero. Thus, we can say that the open and wall boundary conditions were treated independently.

It is worth noting that these two boundary conditions can be satisfied in a unified manner. This aspect simplifies the computation algorithm, making a computational code more practicable. In this paper, we propose a method for the unified treatment of the open and wall boundary conditions based on the semi-Lagrangian scheme and prove that the proposed method yields efficient tidal simulations.

In what follows, we describe the numerical simulation method developed in this study, and present results obtained from applications to some problems of interest. By comparing the results with analytical ones, we discuss the performance of the proposed method in order to provide a basis for improving ocean models.

Governing equations of external mode and derivation of hyperbolic-type equations

The primitive form of the equations governing the dynamics of shallow water on a rotating plane is,

$$\begin{cases} \dfrac{\partial u}{\partial t} + u\dfrac{\partial u}{\partial x} + v\dfrac{\partial u}{\partial y} + g\dfrac{\partial h}{\partial x} = -g\dfrac{\partial z}{\partial x} + fv + E_u, \\ \dfrac{\partial v}{\partial t} + u\dfrac{\partial v}{\partial x} + v\dfrac{\partial v}{\partial y} + g\dfrac{\partial h}{\partial y} = -g\dfrac{\partial z}{\partial y} - fu + E_v, \\ \quad \dfrac{\partial h}{\partial t} + u\dfrac{\partial h}{\partial x} + h\dfrac{\partial u}{\partial x} + v\dfrac{\partial h}{\partial y} + h\dfrac{\partial v}{\partial y} = 0, \end{cases} \tag{1}$$

where (x, y) is a pair whose components respectively represents the eastward and northward axes of the horizontal two-dimensional spatial coordinate system, and t is the time. The notations (h, u, v) are variables, among which u and v are respectively the eastward and northward components of the flow velocity, and h is the water column height. f and g, which are constants denote the Coriolis parameter and gravitational acceleration, respectively. Further, $z = z(x, y)$ is the height of the sea bottom from the reference level; while E_u and E_v are respectively the eastward and northward components of acceleration due to other forces. In this study, we assumed that $(E_u, E_v) = (0, 0)$.

To transform the primitive form, given in Eq. (1), into a form of a hyperbolic-type equation, the terms on the left-hand sides are expressed in the matrix form as,

$$\frac{\partial}{\partial t}\begin{bmatrix} h \\ u \\ v \end{bmatrix} + \mathbf{A}\frac{\partial}{\partial x}\begin{bmatrix} h \\ u \\ v \end{bmatrix} + \mathbf{B}\frac{\partial}{\partial y}\begin{bmatrix} h \\ u \\ v \end{bmatrix} = \mathbf{o}, \tag{2}$$

$$\mathbf{A} \equiv \begin{bmatrix} u & h & 0 \\ g & u & o \\ 0 & 0 & u \end{bmatrix}, \mathbf{B} \equiv \begin{bmatrix} v & 0 & h \\ 0 & v & 0 \\ g & 0 & v \end{bmatrix}.$$

Linearly superimposing $\mathbf{A}$ and $\mathbf{B}$ with the weights n_x and n_y, respectively, a matrix $\mathbf{C}$ is defined as (e.g., [8]),

$$\mathbf{C} \equiv n_x\mathbf{A} + n_y\mathbf{B} = \begin{bmatrix} n_x u + n_y v & n_x h & n_y h \\ n_x g & n_x u + n_y v & 0 \\ n_y g & 0 & n_x u + n_y v \end{bmatrix}, \tag{3}$$

$$n_x + n_y = 1.$$

By changing n_x and n_y, which satisfied Eq. (3), the velocity vectors in the transformed form of Eq.

(1) are rotated.

In this study, the two-dimensional problem is split into two one-dimensional problems: x and y-directional problems. We solved these two problems, sequentially. By setting $\left(n_x, n_y\right) = \left(1, 0\right)$, we obtained the hyperbolic-type equation in the x-direction as,

$$\frac{\partial}{\partial t}\begin{bmatrix} R_x^+ \\ R_x^- \\ v \end{bmatrix} + \Delta_x \frac{\partial}{\partial x}\begin{bmatrix} R_x^+ \\ R_x^- \\ v \end{bmatrix} = \mathbf{o},$$
$$\begin{bmatrix} R_x^+ \\ R_x^- \end{bmatrix} \equiv \begin{bmatrix} \dfrac{g}{c}h + u \\ \dfrac{g}{c}h - u \end{bmatrix},\ \Delta_x \equiv \mathrm{diag}\left(u + c, u - c, u\right), \tag{4}$$

where $c \equiv \sqrt{gh}$ is the phase speed of long wave without the effect of self-rotation of the Earth. R_x^+ and R_x^- represent newly defined variables which are obtained by solving the above one-dimensional hyperbolic-type equations in the x-direction.

On the other hand, by setting the weights $\left(n_x, n_y\right) = \left(0, 1\right)$, we obtained the following one-dimensional hyperbolic-type equations in the y-direction,

$$\frac{\partial}{\partial t}\begin{bmatrix} R_y^+ \\ R_y^- \\ u \end{bmatrix} + \Delta_y \frac{\partial}{\partial y}\begin{bmatrix} R_y^+ \\ R_y^- \\ u \end{bmatrix} = \mathbf{o},$$
$$\begin{bmatrix} R_y^+ \\ R_y^- \end{bmatrix} \equiv \begin{bmatrix} \dfrac{g}{c}h + v \\ \dfrac{g}{c}h - v \end{bmatrix},\ \Delta_y \equiv \mathrm{diag}\left(v + c, v - c, v\right), \tag{5}$$

where R_y^+ and R_y^- are newly defined variables.

The two sets of the three variables, $\left(R_x^+, R_x^-, v\right)$ and $\left(R_y^+, R_y^-, u\right)$, are commonly governed by the hyperbolic-type equations, the solution of which can be determined by identifying the value at the upstream point on the characteristic curves. As the time evolves, the six variables $\left(R_x^+, R_x^-, v\right)$ and $\left(R_y^+, R_y^-, u\right)$ are transported on the characteristic curves (Fig. 1). The velocities with which these variables are transported are equivalent to the eigenvalues of $\mathbf{A}$ and $\mathbf{B}$, written as the diagonal elements of Δ_x and Δ_y, respectively.

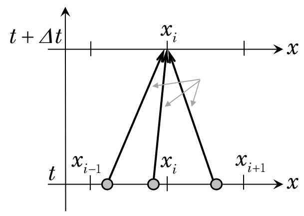

Fig. 1. Schematics of characteristic curves in the *x*-directional. x_{i-1}, x_i, and x_{i+1} are three consecutive points on the *x*-axis. The arrows denote characteristic curves extending from upstream points at time t (gray circles) to the point x_i at time $t+\Delta t$. The symbols "+," "-," and "up" at the upstream points means that the locations of these upstream points are determined by the transportation velocities $u+c$, $u-c$, and u, respectively.

Assuming that the right-hand sides of Eqs. (4) and (5) are zero, that is, that there are no source terms, the six variables remain constant during the transportation (Riemann invariant). The semi-Lagrangian scheme searches the characteristic curves for the point upstream by the transportation distance for a time step.

Among the semi-Lagrangian schemes, in this study, we employed the constraint interpolation profile-conservative semi-Lagrangian 3 (CIP-CSL3) [9] scheme. The split algorithm for solving the 2-D problem considered herein can elicit the excellent accuracy and stability of the scheme. Compared with the Eulerian method with the staggered grid collocation, higher numbers of variables have to be evaluated when the CIP-CSL3 scheme is used (Fig. 2); thus, requiring larger computational memories. However, its outstanding accuracy and stability properties are evident in the simulation of the coastal sea as well as in the benchmarks of computational fluid dynamics studies, to compensate the drawback. We employed the CIP-CSL3 scheme in the *x* and *y*-directional steps. The variables on the upstream points of the western, central, and eastern collocation points are determined in the x-directional step (E, C, and W collocation points in Fig. 2); while the variables on the upstream points of the southern, central, and northern collocation points are determined in the *y*-directional step (S, C, and N collocation points in Fig. 2).

If the source terms such as E_u, E_v, and Coriolis force terms are included in the governing equations—while being transported on the characteristic curves—then the six variables will vary, causing the value at the downstream point to deviate from that at the upstream point. Even in such a situation, an efficient algorithm can be constructed as described in the next section.

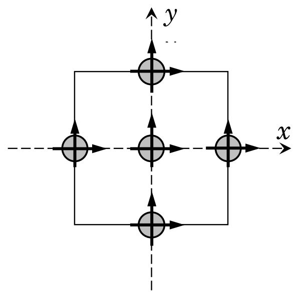

Fig. 2. Western (W), eastern (E), southern (S), northern (N), and central (C) collocation points in a grid. Gray circles represent water column height (h), whereas horizontal and vertical arrows respectively represent eastward (u) and northward (v) components of flow velocity.

An algorithm for numerical computations

Fig. 3 illustrates the flowchart of the time-marching of the variables.

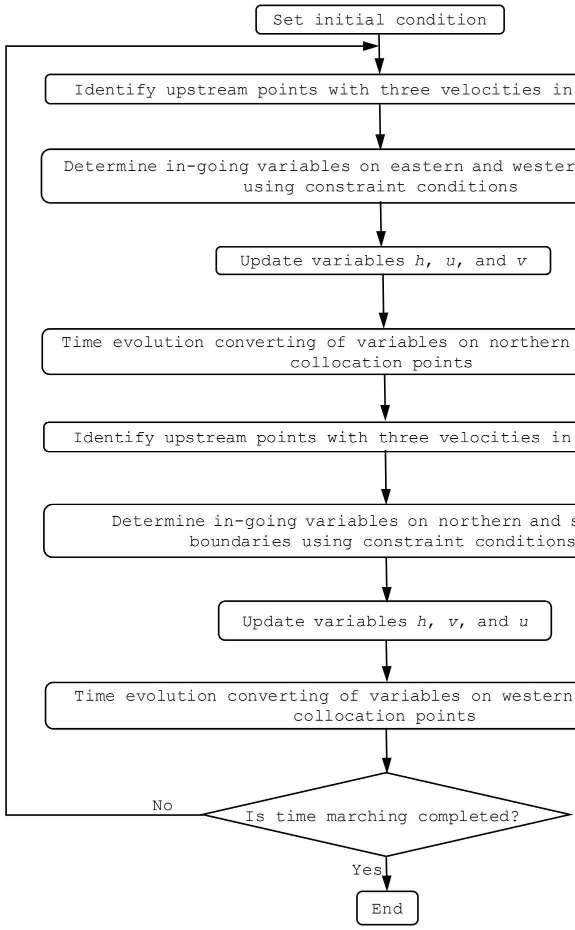

Fig. 3. A flowchart of the algorithm for the time-marching of the variables.

Let values at upstream points in the *x*-direction be indexed by the superscripts "$+$," "$-$," and "up," which mean that the locations of these upstream points are determined by the transportation velocities $u+c$, $u-c$, and u, respectively. Let Δt denotes a discrete time step, and the superscript "$*$" indexes values at a new time step ($t+\Delta t$). The accumulated effect of the Coriolis force in a time step is calculated by the line integration of the Coriolis force on the characteristic curve (Fig. 4), which is approximated in this study using the trapezoid rule (e.g., [4, 10]).

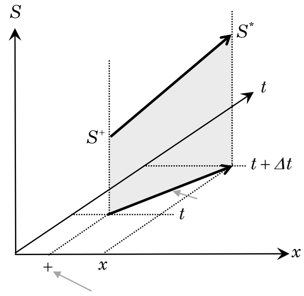

Fig. 4. Schematic view of the integration of source term on the characteristic curve, where S denotes the source term, and the gray square represents the trapezoid approximation of the integration.

The discretized forms of the transformed equation in the *x*-direction are given as,

$$
\begin{aligned}
&\frac{g}{c}\left(h^* - h^+\right) + \left(u^* - u^+\right) = -\frac{g}{u+c}\left(z^* - z^+\right) + \frac{1}{2} f\left(v^* + v^+\right)\Delta t, \\
&\frac{g}{c}\left(h^* - h^-\right) - \left(u^* - u^-\right) = \ \frac{g}{u-c}\left(z^* - z^-\right) - \frac{1}{2} f\left(v^* + v^-\right)\Delta t, \\
&v^* - v^{\mathrm{up}} = -\frac{1}{2} g\left\{\left(\frac{\partial z}{\partial y}\right)^{\mathrm{up}} + \left(\frac{\partial z}{\partial y}\right)^{*}\right\}\Delta t - \frac{1}{2} f\left(u^* + u^{\mathrm{up}}\right)\Delta t.
\end{aligned}
\tag{6}
$$

Once all the upstream values are determined, the values h^*, u^*, and v^* at a new time step, are updated by the following algebraic formulas,

$$
\begin{cases}
h^* = \dfrac{c}{2g}\left(U^+ + U^-\right), \\
u^* = \dfrac{1}{2\left\{1 + \dfrac{1}{4}\left(f\Delta t\right)^2\right\}}\left(U^+ - U^- + fv'\Delta t\right), \\
v^* = v_{\mathrm{up}} - \dfrac{1}{2} g\left\{\left(\dfrac{\partial z}{\partial y}\right)^{\mathrm{up}} + \left(\dfrac{\partial z}{\partial y}\right)^{*}\right\}\Delta t - \dfrac{1}{2} f\left(u^* + u^{\mathrm{up}}\right)\Delta t,
\end{cases}
\tag{7}
$$

where the new notations are defined as follows:

$$
\begin{cases}
U^{+} \equiv \dfrac{g}{c} h^{+} + u^{+} - \dfrac{g}{u+c}\left(z^{*} - z^{+}\right) + \dfrac{1}{2} f v^{+} \Delta t, \\
U^{-} \equiv \dfrac{g}{c} h^{-} - u^{-} + \dfrac{g}{u-c}\left(z^{*} - z^{-}\right) - \dfrac{1}{2} f v^{-} \Delta t, \\
v' \equiv v^{\mathrm{up}} - g \dfrac{1}{2}\left\{ \left(\dfrac{\partial z}{\partial y}\right)^{\mathrm{up}} + \left(\dfrac{\partial z}{\partial y}\right)^{*} \right\} \Delta t - \dfrac{1}{2} f u^{\mathrm{up}} \Delta t.
\end{cases}
\tag{8}
$$

The discretized forms for the y-directional equations are derived in the same manner as those for the x-directional ones, and are thus obtained as,

$$
\begin{aligned}
&\frac{g}{c}\left(h^{*} - h^{+}\right) + \left(v^{*} - v^{+}\right) = -\frac{g}{v+c}\left(z^{*} - z^{+}\right) - \frac{1}{2} f\left(u^{*} + u^{+}\right)\Delta t, \\
&\frac{g}{c}\left(h^{*} - h^{-}\right) - \left(v^{*} - v^{-}\right) = \frac{g}{u-c}\left(z^{*} - z^{-}\right) + \frac{1}{2} f\left(u^{*} + u^{-}\right)\Delta t, \\
&u^{*} - u^{\mathrm{up}} = -\frac{1}{2} g \left\{ \left(\frac{\partial z}{\partial x}\right)^{\mathrm{up}} + \left(\frac{\partial z}{\partial x}\right)^{*} \right\} \Delta t + \frac{1}{2} f\left(v^{*} + v^{\mathrm{up}}\right)\Delta t.
\end{aligned}
\tag{9}
$$

The superscripts "+," "–," and "up" are used to distinguish the upstream points whose locations are determined by the transportation velocities $v+c$, $v-c$, and v in the y-direction, respectively. The variables are updated using the following formulas,

$$
\begin{cases}
h^{*} = \dfrac{c}{2g}\left(V^{+} + V^{-}\right), \\
v^{*} = \dfrac{1}{2\left\{1 + \dfrac{1}{4}\left(f \Delta t\right)^{2}\right\}}\left(V^{+} - V^{-} - f u' \Delta t\right), \\
u^{*} = u_{\mathrm{up}} - \dfrac{1}{2} g \left\{ \left(\dfrac{\partial z}{\partial x}\right)^{\mathrm{up}} + \left(\dfrac{\partial z}{\partial x}\right)^{*} \right\} \Delta t + \dfrac{1}{2} f\left(v^{*} + v^{\mathrm{up}}\right)\Delta t,
\end{cases}
\tag{10}
$$

where the new notations in the above equations are defined as

$$
\begin{cases}
V^{+} \equiv \dfrac{g}{c}h^{+} + v^{+} - \dfrac{g}{v+c}\left(z^{*} - z^{+}\right) - \dfrac{1}{2} f u^{+} \Delta t, \\
V^{-} \equiv \dfrac{g}{c}h^{-} - v^{-} + \dfrac{g}{v-c}\left(z^{*} - z^{-}\right) + \dfrac{1}{2} f u^{-} \Delta t, \\
u' \equiv u^{\mathrm{up}} - g\dfrac{1}{2}\left\{\left(\dfrac{\partial z}{\partial x}\right)^{\mathrm{up}} + \left(\dfrac{\partial z}{\partial x}\right)^{*}\right\}\Delta t + \dfrac{1}{2} f v^{\mathrm{up}} \Delta t.
\end{cases}
\tag{11}
$$

Time evolution converting

The preceding section presents methods for updating the variables h, u, and v separately in the x and y-directions. The proposed algorithm, i.e., the directional splitting algorithm, is a kind of fractional time evolution algorithm, in which an auxiliary step is needed to ensure that the time marching of all the variables is aligned before each of the directionally-split algorithms begins.

In the x-directional evolution step, only the three variables collocated at the western, central, and eastern collocation points (W, C, and E collocation points in Fig. 2) are evolved (Eq. 7), while the two variables collocated at the southern and northern points (S and N collocation points in Fig. 2) are left unchanged. After the time evolutions of the center, east, and west variables are terminated, the southern and northern variables are evolved by linear interpolation of two neighboring variables at the center point (The box NS in Fig. 5), which is referred to as time evolution converting in [11]. Similarly, in the y-directional evolution step, after the temporal evolutions of h, v, and u by Eq. (10), the variables collocated at the western and eastern points need to be evolved by the linear interpolation (The box EW in Fig. 5). An interpolation at the northern point is given by,

$$
\Delta_x \phi^{\mathrm{N}}_{i,j+\frac{1}{2}} = \frac{1}{2}\left(\Delta_x \phi^{\mathrm{C}}_{i,j} + \Delta_x \phi^{\mathrm{C}}_{i,j+1}\right),
\tag{12}
$$

where $\Delta_x \phi^{\mathrm{C}}_{i,j}$ is an increment of the variable ϕ at the central point $(i,\, j)$ during an x-directional time evolution step, and $\Delta_x \phi^{\mathrm{N}}_{i,j+\frac{1}{2}}$ is an increment of the same variable ϕ at the northern point during the same step. The interpolation at the southern point is given in a similar manner as that at the northern point. The interpolation at the eastern point is given by,

$$
\Delta_y \phi^{\mathrm{E}}_{i+\frac{1}{2},j} = \frac{1}{2}\left(\Delta_y \phi^{\mathrm{C}}_{i,j} + \Delta_y \phi^{\mathrm{C}}_{i+1,j}\right),
\tag{13}
$$

where $\Delta_y\phi^{\mathrm{C}}_{i,j}$ is an increment of the variable ϕ at the central point $(i,\,j)$ during a y-directional time evolution step, and $\Delta_y\phi^{\mathrm{E}}_{i+\frac{1}{2},j}$ is an increment of the same variable ϕ at the eastern point during the same step. The interpolation at the western point is written in a similar manner as that at the eastern point.

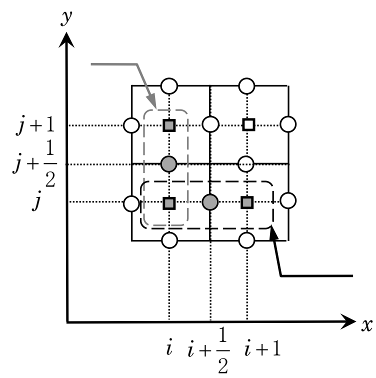

Fig. 5. Collocation points referred to during time evolution converting. After x and y-directional steps are terminated, the variables on the gray circle in boxes NS and EW, respectively are updated by linear interpolation using variables on the collocation points C.

The imposition of wall and open boundary conditions

Variables traveling toward the open or wall boundary from the inner region, referred to as out-going variables, can be determined by semi-Lagrangian scheme; however, variables traveling from the outer region into the inner region, referred to as in-going variables, cannot be determined by identifying their upstream points because the upstream points are located outside the computational region (Fig. 6).

Therefore, we determined the in-going variables using relations that constrain the variables to satisfy the boundary conditions. Once the unknown parameters on the boundary are determined, the updated formulas (Eqs. 7 and 10) can be applied regardless of the locations of the grid (whether in the inner region or on the boundary) and the types of boundary conditions (wall or open).

This universal handling of the evolving variables owes to the collocation of the normal velocity and water column height variables at the same point—it differs from the staggered collocation (e.g., [12-15]) with the velocity and water column height arranged at different points. The staggered collocation requires that only grid widths near the open boundary should be treated specially (e.g., [13-14]), which nevertheless, can allow the wave with the phase speed of $\sqrt{gh}$ only to be transparent; whereas the collocation employed in this study allows the passage of all types of waves without reflection.

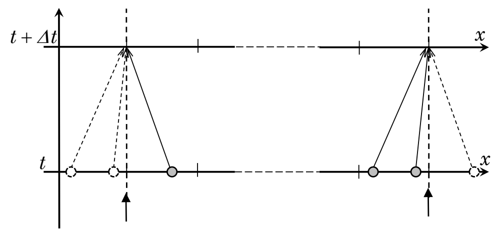

Fig. 6. Schematics of methods for determining in-going variables on open and wall boundaries in the x-directional step. The characteristic curves as solid arrows originate from upstream points inside a computational domain (gray circles), and the ones as dashed arrows originate from an upstream point outside the domain (dashed circle).

Constraint relation for wall boundary condition

The constraint relation among the variables on the wall boundary is determined such that the component of the velocity normal to the wall vanishes at that point. The constraint relation in the x-direction is given by,

$$0 = U^{+} - U^{-} + fv'\Delta t \,, \tag{14}$$

and the one in the y-direction is given by,

$$0 = V^{+} - V^{-} - fu'\Delta t \,. \tag{15}$$

The in-going variables on the wall boundaries are specified using these relations.

Constraint relation for open boundary condition

This subsection explains the method for determining the in-going variables (Fig. 6) by deriving constraint relations among the variables based on a fundamental physical law. Waves propagating from the inner region must pass through the open boundary without producing unnatural reflections. To this end, in [13-14], the authors presented a simple and reliable method based on the physical law of fixed end reflection of wave: a virtual wall is first placed along the open boundary, and the water column height is computed once. Following this law, the presence of the virtual wall makes the displacement of the water surface on the wall twice as high as that of the transmitted wave. Hence, the displacement of the transmitted wave can be calculated by halving the displacement of the wave determined in the presence of the virtual wall.

The constraint relations among the variables which satisfy the open boundary condition are obtained by equating the displacement of the transmitted wave, computed based on the method discussed above, with the displacement of the water surface at the new time step. By denoting the water column height under the calm state by h_0, and the displacement of the water surface by an incident wave propagating from the outer region by η_1, the constraint relations are expressed as,

$$U^{+} = -\frac{1}{2} f v' \Delta t + \frac{g}{c}\left(h_0 + 2\eta_1\right), \tag{16}$$

on the western open boundary, and

$$U^{-} = \frac{1}{2} f v' \Delta t + \frac{g}{c}\left(h_0 + 2\eta_1\right), \tag{17}$$

on the eastern open boundary.

For the northern and southern open boundaries, the constraint relations in the *y*-direction are;

$$V^{+} = \frac{1}{2} f u' \Delta t + \frac{g}{c}\left(h_0 + 2\eta_1\right), \tag{18}$$

on the southern open boundary, and

$$V^{-} = -\frac{1}{2} f u' \Delta t + \frac{g}{c}\left(h_0 + 2\eta_1\right), \tag{19}$$

on the northern open boundary.

Applications of the proposed method

Propagation of shallow water wave on undulating sea bottom topography

The semi-Lagrangian code implemented in this study is first applied to a shallow water wave propagation on an undulating sea bottom topography (Fig. 7). Under the assumption that the steepness of the topography and the amplitude of incident wave are small, we obtained an approximated analytical solution of the wave with a perturbation technique (Appendix A), and compared it with numerical results obtained by the method proposed in this study. Table 1 shows a list of the parameters for this numerical computation.

Table 1. List of parameters for numerical computation of propagation on an undulating sea bottom topography.

Time step	2.0 sec
Grid length	$2.8*10^2$ m
Dimension of area	$1.4*10^4$ m
Coriolis parameter	0.0 sec^{-1}

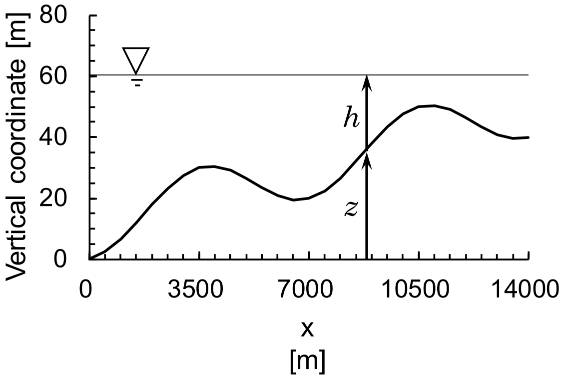

Fig. 7. Vertical coordinate of sea bottom topography (z). The water column height (h) is illustrated as the distance from : to the water surface.

Transparency of waves through an open boundary

To check the effectiveness and efficiency of the proposed method for imposing an open boundary condition, we applied it is applied to one-dimensional (1-D) and two-dimensional (2-D) waves propagating and passing through open boundaries. In the 1-D problem (Fig. 8), at one boundary, a sinusoidal incident wave is specified, and at the other boundary, the open boundary condition is imposed. In the 2-D problem (Fig. 9), at the western and southern boundaries, a sinusoidal incident wave is specified in a direction oblique to the x and y-axes. We performed two simulations for small and large sizes of computational domains in both the 1-D and 2-D problems. Further, we examined the wave transparency by comparing the results of the two simulations.

Table 2. List of parameters for one-dimensional numerical computation of the transparency of waves at an open boundary.

	Small domain	Large domain
Time step	6.0 sec	
Grid length	4.0×10^3 m	
Dimension of area	8.0×10^5 m	2.4×10^6 m
Water depth	50.0 m	
Coriolis parameter	0.0 sec^{-1}	

Period of incident wave	4.47×10^4 sec
Amplitude of incident wave	0.30 m

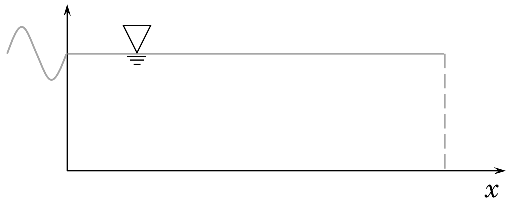

Fig. 8. Schematics of the one-dimensional domain. Sinusoidal time variation of the water surface is specified at the left-end, and open boundary condition is imposed at the right-end.

Table 3. List of parameters for two-dimensional numerical computation of the transparency of waves at an open boundary.

	Small domain	Large domain
Time step	6.0 sec	
Grid length in *x*- and *y*-directions	4.0×10^3 m and 4.0×10^3 m,	
Dimensions of area in *x*- and *y*-directions	8.0×10^5 m and 8.0×10^5 m	2.4×10^6 m and 2.4×10^6 m
Water depth	50.0 m	
Coriolis parameter	0.0 sec^{-1}	
Direction of incident wave	45°	
Period of incident wave	4.47*10^4 sec	
Amplitude of incident wave	0.30 m	

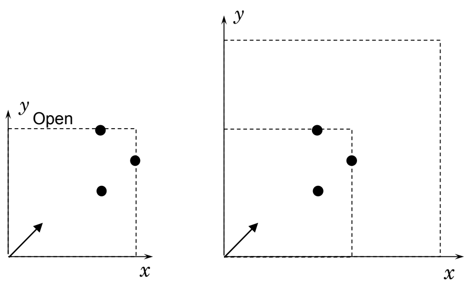

Fig. 9. Schematic views of small (left figure) and large (right figure) two-dimensional domains. Waves are incident obliquely from western and southern boundaries. Arrows denote the wavenumber vector of this wave. The letters “a”, “b”, and “c” indicate the points where results of the small and large domains are compared.

Tides in a semi-enclosed rectangular bay

We examined the performance of the proposed method in tidal simulation by conducting numerical computations for tides in a semi-enclosed bay with a rectangular coastal topography, (Fig. 10) (Taylor problem, [16]). The idealized configuration of the coast and the linearization of the shallow water model allow us to express the tidal dynamics solution analytically (Appendix B), which we compared with the numerical results to verify the effectiveness and efficiency of the method.

Table. 4 List of parameters for two-dimensional numerical computation of tides in a semi-enclosed rectangular bay.

Time step	6.0 sec
Grid lengths in x-, and y-direction	5.0×10^3 m, and 5.0×10^3 m
Dimensions of area in x-, and y-direction	1.0×10^6 m, and 0.6×10^6 m
Water depth	50.0 m
Coriolis parameter	1.2×10^{-4} sec^{-1}
Period of incident wave	4.4712×10^4 sec
Amplitude of incident wave	0.30 m

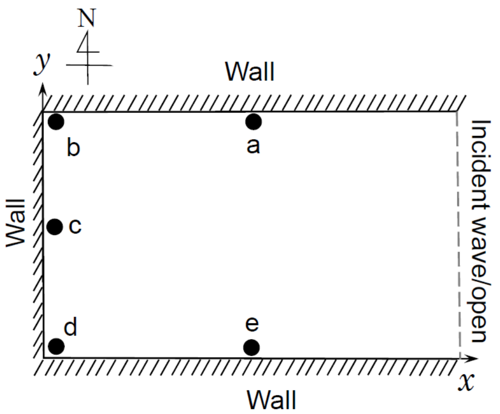

Fig. 10. Schematics of a semi-enclosed rectangular bay. A sinusoidal time variation is imposed as tidal wave incidence on the eastern boundary. The open boundary condition is imposed on the eastern boundary. The closed circles (a-e) indicates the points at which results of numerical and analytical calculations are compared in Fig. 16.

Results and discussion

Propagation of shallow water wave on an undulating sea bottom topography

This problem can be used as a benchmark to check the ability of numerical computation methods (e.g., [17-18, 3]).

The analytical solution has two local maxima of the water flow velocity (Fig. 11), which are formed through the interference of the bottom mounts with the water flows. As these flows are being formed, the water column height varies uniformly in the entire computational domain at the period of the incident wave. The numerical computation captured these shapes and time variations.

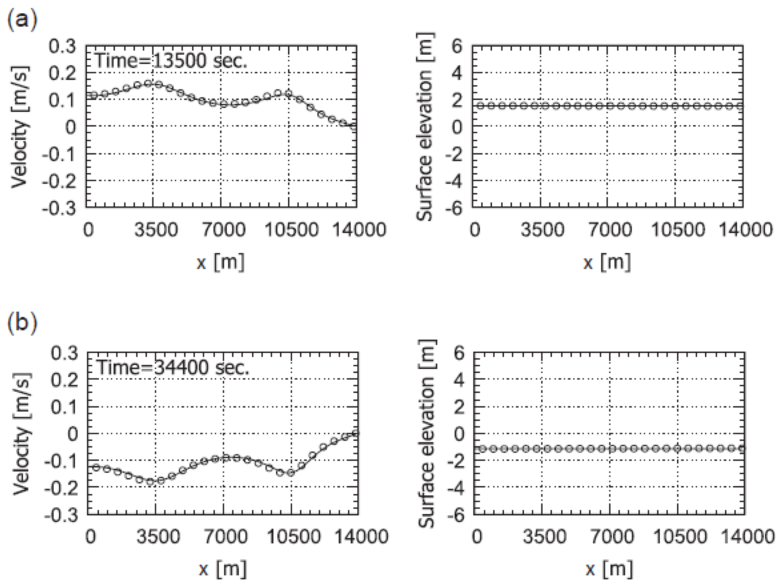

Fig. 11. Snapshots of flow velocity and surface elevation at times 13500 sec and 34400 sec. Solid lines denote analytical results, while opened circles indicate numerical results.

The analytical result shows that the velocity is uniformly distributed similarly as the water column height, while its sign changes at the period of the incident wave. Additionally, the two local maxima and minima of the velocity are formed during flood and ebb tides, respectively. These features of the analytical result are accurately simulated by the numerical computation.

The agreements of the numerical results with the analytical ones demonstrate that the method proposed in this study can efficiently estimate the tidal mechanics. In particular, it can appropriately capture the effect of the undulation of the sea bottom topography on the water flow.

Transmission of waves through an open boundary

If the scheme for the open boundary properly works, the sinusoidal wave entering at $x = 0$ m is expected to pass through the point $x = 8.0 \times 10^5$ m where the open boundary is placed in the small domain (Fig. 12). The water column height in the small domain is sinusoidal with the same period and amplitude as those in the incident wave and conforms with those in the large domain.

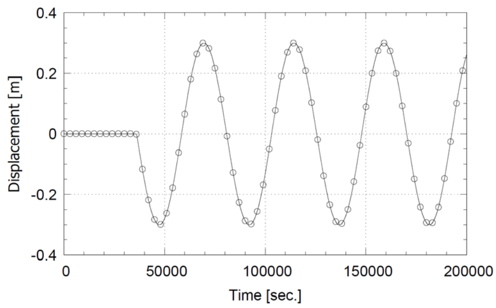

Fig. 12. Temporal evolutions of water surface elevation measured from the water surface height under the calm state. The solid line represents the result at $x = 8.0 \times 10^5$ m in the large domain, While the open circles are the result at $x = 8.0 \times 10^5$ m, the left-end of the small domain.

The 1-D calculation considers the wave propagation in the same direction as the characteristic curve, allowing the open boundary scheme to exhibit the desirable performance easily. However, a more rigorous test is required to test the scheme. Thus, a 2-D computation was performed to examine if the proposed open boundary scheme applies to waves approaching from an oblique direction. At the southern and western boundaries, a sinusoidal wave is an incident in the direction of 45° from the x-axis. The wave direction, in this case, differs from the directions of both the characteristic curves in the x and y-directional steps. In the same manner, as in the 1-D computations, the 2-D computations were performed for the small and large domains.

In the simulation for the small domain, the wave phase obliquely propagates in the north-eastern direction (Fig. 13). The configurations of the water surface were consistent with the corresponding ones in the large domain (Fig. 14). This shows that the wave propagation yielded by the two computations are equivalent.

The results obtained demonstrate that the scheme for imposing the open boundary condition enables waves arriving the boundary to pass through without being unnaturally reflected and deformed; moreover, this desirable performance occurs whether the direction of wave propagation matches the directions of characteristic curves or not.

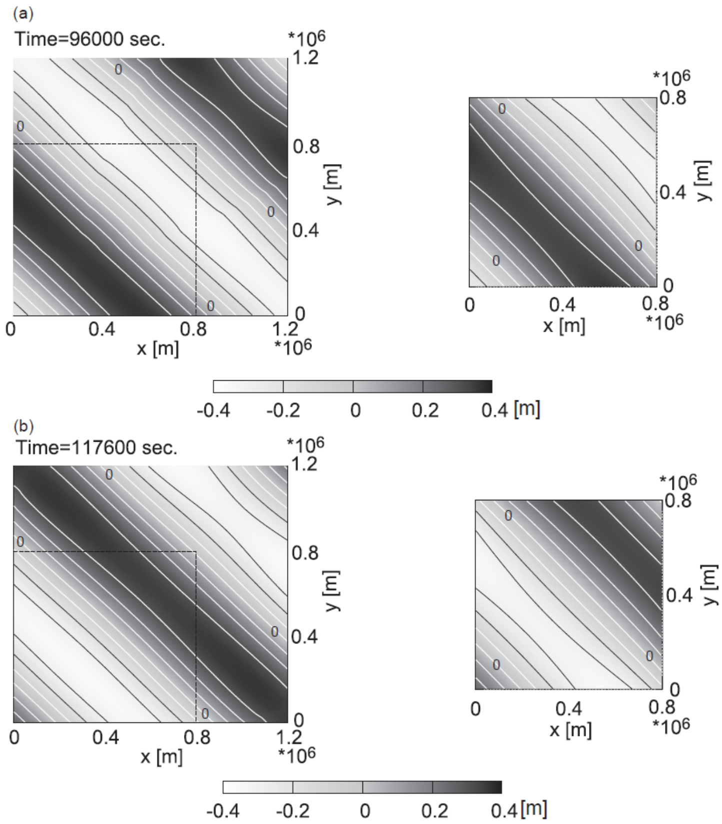

Fig. 13. Distributions of water surface elevation measured from the water surface height under the calm state at (a) $t = 96000$ sec and (b) $t = 117600$ sec. Left and right panels are results of the large and small domain simulations, respectively. The dashed lines in the large domain correspond to the northern and eastern boundaries of the small domain. The contour interval is 0.1 m.

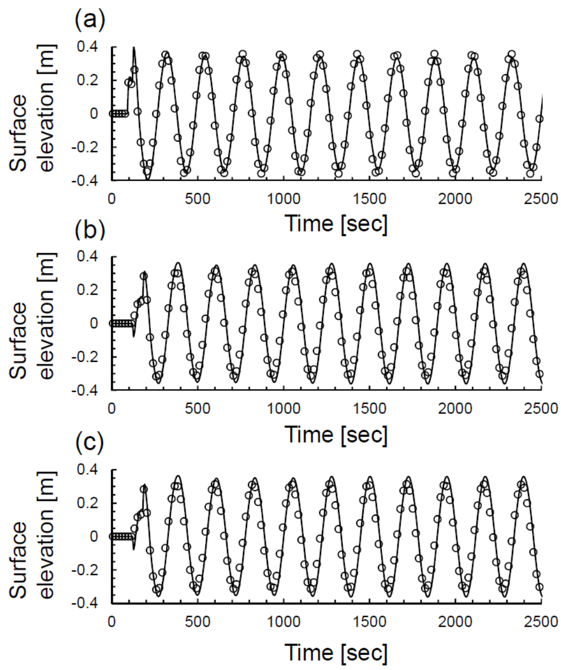

Fig. 14. Temporal evolutions of water surface elevation measured from the water surface height under the calm state at (a) point a; (b) point b, and (c) point c in Fig. 9. Solid lines and open circles denote the result of the large and small domain simulations, respectively.

Tides in a semi-enclosed rectangular bay

The bay addressed in this study has the same order of spatial dimensions as the Rossby deformation radius (1.84×10^6 m). In this spatial scale, the tidal wave in the bay is expected to behave as the Kelvin wave mostly, its excellent simulation performance is the objective of this subsection.

The analytical procedure for the rectangular bay (Appendix B) includes the two modes (westward and eastward) of the Kelvin wave and multiple modes of the Poincaré wave. The disturbances of water surface move westward along the northern coastline, and eastward along the southern coastline (left panels of Fig. 15). The Kelvin wave theory can explain this spatial-temporal pattern. For the present case, the amplitudes of the Poincaré wave modes are quite smaller than those of the Kelvin wave modes.

In the numerical results, at a short time after its incidence on the eastern boundary, the disturbances occur uniformly from the north edge to the south edge of the eastern boundary, then begin to move westward along the northern coastline, turn to the south after arriving at the western boundary, and subsequently moves eastward along the southern coastline. The travel path trapped to the coast computed numerically is consistent with that computed analytically.

However, the response, as mentioned above for a short time just after the incidences in the numerical result, is not seen in the analytical result. The analytical procedure (Appendix B) considers the forced oscillation component only, while it excludes the transient component which prevails for a short time just after the incidences of water surface movement at the eastern boundary.

A comparison of the numerical and analytical results demonstrates that the former reasonably agree with the latter in the following respects: the wavelength in the propagation direction, phase of the propagation, the evanescence of disturbances toward the offshore, and the locations of amphidromic points where the water surface disturbances occur minimally.

Tidal ellipses obtained from the numerical and analytical calculations (Fig. 16) are compared at the points indicated in Fig. 10. The lengths and directions of the major and minor axes reasonably well agree between the numerical and analytical calculations.

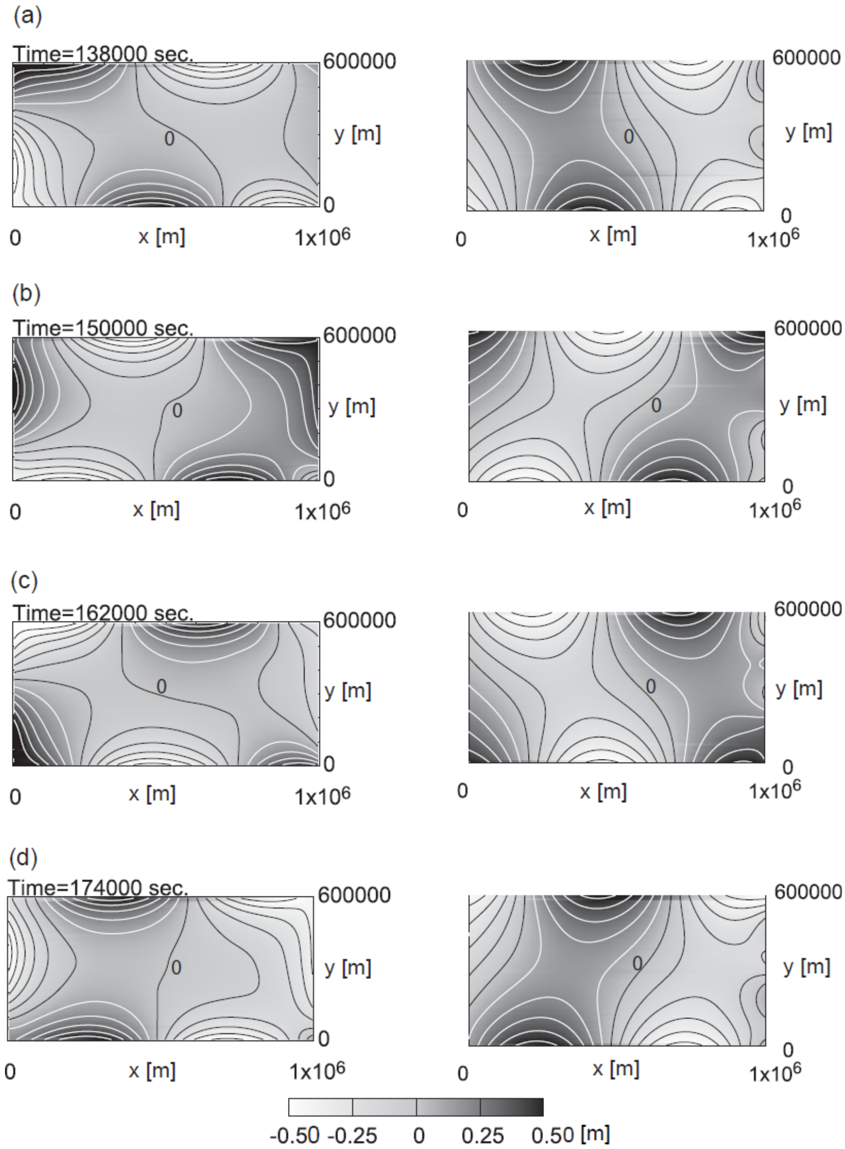

Fig. 15. Snapshots of water surface elevations measured from the water surface height under the calm state at (a) $t = 138000$ sec, (b) $t = 150000$ sec, (c) $t = 162000$ sec, and (d) $t = 174000$ sec. Left and right panels are numerical and analytical results, respectively. The contour interval is 0.1 m.

The employment of the semi-Lagrangian scheme enables one to capture the coastally trapped propagation of waves with few numerical dissipations and to conduct the numerical computations stably. This result allows us to conclude that the proposed method could be utilized to simulate the external mode of marine dynamics.

Nevertheless, this study has some limitations which we briefly highlight here. In this study, the verification of the numerical computation method was performed by addressing a straightforward problem. Moreover, the performance of the proposed method should be compared with observed results; however, we will consider this in a future study of our project. This study addresses the external mode of marine dynamics only but excluded the internal mode. It should be noted that the algorithm constructed in this study can be combined with an algorithm for solving the internal mode. In a coupled external-internal computation, the external force terms $\left(E_u, E_v\right)$ will be activated.

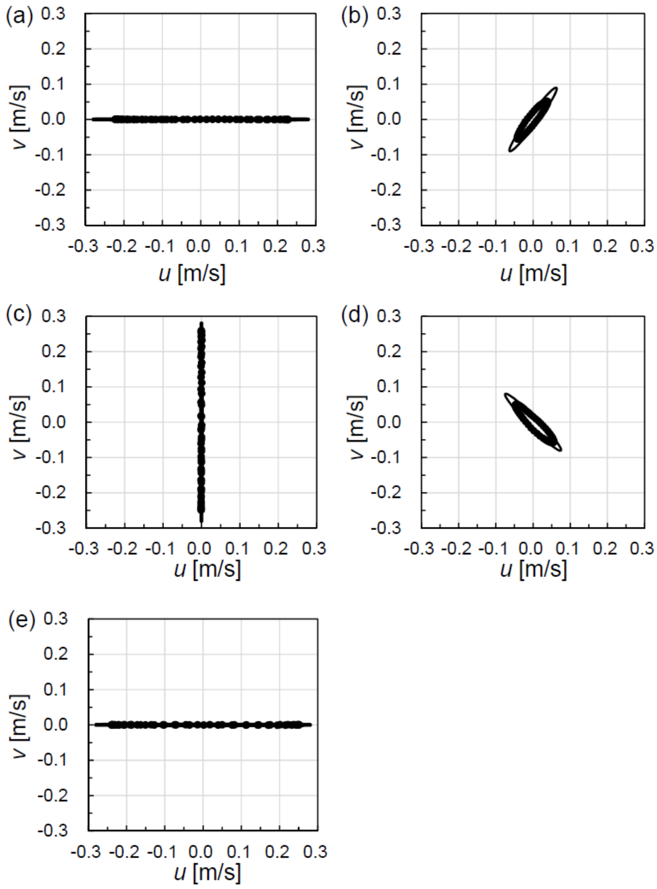

Fig. 16. Tidal ellipses obtained from numerical (closed circles) and analytical (solid lines) calculations. Panels (a) through (e) correspond to the points "a" through "e" indicated in Fig. 10, respectively.

Conclusion

This study constructed a numerical computation method of shallow water equation with Coriolis effect to simulate tides. The method adopted a semi-Lagrangian scheme to solve the hyperbolic form of the shallow water model, providing more accurate and stable computations than the traditional finite-difference schemes. Additionally, a new semi-Lagrangian treatment for realizing no unnatural reflections on open boundaries are incorporated into the method. By applying the proposed method to some problems, this study drew the following conclusions:

1. The implemented semi-Lagrangian scheme accurately computes the solution of the shallow water model.

2. An exact imposition of the open boundary condition is realizable by applying the non-reflective

scheme in the framework of the semi-Lagrangian scheme.

3. The proposed method is applicable to tidal simulations of semi-enclosed bays.

Appendix A:

The mathematical treatment for obtaining the analytical solution in [17] is briefly described here.

By applying the perturbation technique, the solution of the 1-D shallow water equation can be mathematically obtained under the assumption that the Froude number F is small.

The initial condition is given as;

$$\begin{cases} h(x, t=0) = H(x), \\ u(x, t=0) = 0, \end{cases}$$

where $H(x)$ is the water depth in the calm state. The boundary condition is;

$$\begin{cases} h(x=0, t) = \varphi(t), \\ u(x=L, t) = 0. \end{cases}$$

The variables (water column height and flow velocity) are asymptotically expanded as power series of the bookkeeping parameter F in the following manner,

$$\begin{cases} h = h_0 + F h_1 + F^2 h_2 + \cdots, \\ u = u_0 + F u_1 + F^2 u_2 + \cdots. \end{cases}$$

Substituting these perturbation expansions into the governing equations, equating the coefficients with the same powers of F, we have the partial differential equations with respect to the expansion coefficients $(h_0, h_1, h_2, \cdots, u_0, u_1, u_2, \cdots)$. Further, the solution of the zeroth-order is given by;

$$\begin{cases} h_0(x,t) = \varphi(t) + H(x), \\ u_0(x,t) = \dfrac{1}{h_0(x,t)} \left\{ -(x-L)\varphi'(t) \right\}. \end{cases}$$

The benchmark problem in this study assumes the incidence of a sinusoidal wave at $x = 0$ m,

$$\varphi(t) = H(0) + dH \left\{ 1 - \sin\left(\frac{2\pi}{T} t + \frac{\pi}{2} \right) \right\},$$

where the amplitude of the incident wave is $dH = 4.00$ m, and its period is $T = 43200.0$ s.

Another assumption of the benchmark is the topographic undulation expressed by the sinusoidal function as,

$$H(x) = A - B\frac{x}{L} - C\sin\left(\frac{4\pi}{L} x - \frac{\pi}{2} \right),$$

where $(A, B, C) = (50.5\,\mathrm{m}, 40.0\,\mathrm{m}, 10.0\,\mathrm{m})$.

Appendix B:

The linearized shallow water equation is solvable by mathematical techniques (e.g., [16, 19]). In this study, the solution was obtained assuming a constant water depth, denoted by h_0. The modeled bay (Fig. 10) is rectangular with an open boundary along $x=0$, and coasts along $x=L$, $y=0$, and $y=B$. The variables are assumed to have a common frequency, σ, as expressed by the equation: $(\eta,u,v)=\mathrm{Re}\left\{(\hat{\eta},\hat{u},\hat{v})e^{i\sigma t}\right\}$, where $(\hat{\eta},\hat{u},\hat{v})$ are the complex amplitudes.

The applications of the variable separation and eigenfunction expansion methods yield the solution comprising four modes: positive Kelvin and Poincaré modes, and negative Kelvin and Poincaré modes. Here the terms "positive" and "negative" indicate wave propagations in positive and negative *x*-directions, respectively. Though the theoretically exact solution requires the superimposition of infinite numbers of Poincaré modes, the computations in this study truncate the number maximally at N.

The complex amplitudes of the positive Kelvin and Poincaré modes are

$$\begin{cases} \hat{\eta}=\dfrac{h_0 k}{\sigma}a, \\ \hat{u}=-a\,e^{\alpha y}e^{ikx}, \\ \hat{v}=0, \end{cases}$$

and

$$\begin{cases} \hat{\eta}=\displaystyle\sum_{n=1}^{N}\kappa_n\left\{C_n\cos(\gamma_n y)+D_n\sin(\gamma_n y)\right\}e^{il_n x}, \\ \hat{u}=\displaystyle\sum_{n=1}^{N}\kappa_n\left\{A_n\cos(\gamma_n y)+B_n\sin(\gamma_n y)\right\}e^{il_n x}, \\ \hat{v}=\displaystyle\sum_{n=1}^{N}\kappa_n\sin(\gamma_n y)e^{il_n x}, \end{cases}$$

respectively.

The complex amplitudes of the negative Kelvin and Poincaré modes are

$$\begin{cases} \hat{\eta}=\dfrac{h_0 k}{\sigma}b\,e^{-\alpha y}e^{-ikx}, \\ \hat{u}=be^{-\alpha y}e^{-ikx}, \\ \hat{v}=0, \end{cases}$$

and

$$\begin{cases} \hat{\eta} = \sum_{n=1}^{N} \lambda_n \left\{ C_n \cos(\gamma_n y) - D_n \sin(\gamma_n y) \right\} e^{-il_n x}, \\ \hat{u} = \sum_{n=1}^{N} \lambda_n \left\{ -A_n \cos(\gamma_n y) + B_n \sin(\gamma_n y) \right\} e^{-il_n x}, \\ \hat{v} = \sum_{n=1}^{N} \lambda_n \sin(\gamma_n y) e^{-il_n x}. \end{cases}$$

The notations (A_n, B_n, C_n, D_n) in the Poincaré modes are defined as

$$\begin{aligned} A_n &= \frac{-\gamma_n l_n \left(-1 + f'^2\right)}{i\left(\gamma_n^{\,2} + l_n^{\,2} f'^2\right)}, \\ B_n &= \frac{f'\left(l_n^{\,2} + \gamma_n^{\,2}\right)}{i\left(\gamma_n^{\,2} + l_n^{\,2} f'^2\right)}, \\ C_n &= \frac{ih_0}{\sigma} \frac{\left(l_n^{\,2} + \gamma_n^{\,2}\right) p}{\gamma_n^{\,2} + l_n^{\,2} f'^2}, \\ D_n &= \frac{ih_0}{\sigma} \frac{\left(l_n^{\,2} + \gamma_n^{\,2}\right) f' l_n}{\gamma_n^{\,2} + l_n^{\,2} f'^2}, \end{aligned}$$

where $f' \equiv f/\sigma$ is a dimensionless Coriolis parameter normalized by the frequency σ.

The y-component of the wavenumber of Poincaré modes is forced to have discrete values by the condition that the bay is bounded along $y = 0$ and $y = B$, written as,

$$\gamma_n = \frac{n}{B}\pi.$$

The x and y-components of the wavenumber (l_n, γ_n) of the Poincaré modes are related to the frequency (dispersion relation) as follows;

$$\begin{aligned} \gamma_n^{\,2} &= -l_n^{\,2} + k^2\left(1 - f'^2\right), \\ k &\equiv \frac{\sigma}{\sqrt{gh_0}}. \end{aligned}$$

Here, α defined as

$$\alpha \equiv \frac{f}{\sqrt{gh_0}} = k f',$$

is the inverse of the Rossby radius of deformation.

References

[1] Blumberg AF, Mellor GL (1987) A description of a three-dimensional coastal ocean circulation model, Heaps N.S. (Ed.), Three-dimensional coastal ocean models, American Geophysical Union, Washington, D.C., pp. 1-16.

[2] Chen, C, Haung H, Beardsley RC, Xu Q, Limeburner R, Gowles GW, Sun Y, Qi J, Lin H (2011) Tidal dynamics in the Gulf of Maine and New England Shelf: An application of FVCOM., J Geophys Res 116 C12010.

[3] Xing Y, Shu CW (2005) High order finite difference WENO schemes with the exact conservation property for the shallow water equations, J Comput Phys, 208:206-227.

[4] Yabe T, Ogata Y (2010) Conservative semi-Lagrangian CIP technique for the shallow water equations, Comput Mech, 46:125-134.

[5] Orlanski I (1976) A simple boundary condition for unbounded hyperbolic flows, J Comput Phys 21(3):251-269.

[6] Hino M (1988) Review-on numerical scheme of non-reflection and free-transmission open boundary, Tech Rep Dept Civil Eng, Tokyo Inst Tech 39:1-5.

[7] Chapman DC (1985) Numerical treatment of cross-shelf open boundaries in a barotropic coastal ocean model, J Phys Oceanogr 15:1060-1075.

[8] Akoh, R, Ii S, Xiao F (2008) A CIP/multi-moment finite volume method for shallow water equations with source terms, Int J Numeric Methods in Fluids 56:2245-2270.

[9] Xiao F, Yabe T (2001) Completely conservative and oscillationless semi-Lagrangian schemes for advection transportation, J Comput Phys 170:498-522.

[10] Hoffman JD (1992) Numerical Methods for Engineers and Scientists, McGraw-Hill.

[11] Xiao F, Yabe T, Peng X, Kobayashi H (2002) Conservative and oscillation-less atmospheric transport schemes based on rational functions, J Geophys Res, 107(D22):4609.

[12] Arakawa A, Lamb VR (1977) Computational design of the basic dynamical processes of the UCLA general circulation model. Methods in Comput Phys: Advances in Res and Appl 17:173-265.

[13] Hino M (1987) A very simple numerical scheme of non-reflection and complete transmission condition of waves for open boundaries, Tech Rep Dept Civil Eng, Tokyo Inst Tech 38:31-38.

[14] Hino M, Nakaza E (1987) Numerical examination of a new non-reflective boundary condition for a computer simulation of hydraulic wave phenomena, Tech Rep Dept Civil Eng, Tokyo Inst Tech 38:39-50.

[15] Fujino M, Kagemoto H, Tabeta S, Hamada T (1994) On the usefulness of non-reflective boundary conditions for a numerical simulation of tide and tidal current, J Soc Naval Archit Japan, 175:161-169.

[16] Fang Z, Ye A, Fang G (1991) Solutions of tidal motions in a semi-enclosed rectangular gulf with open boundary condition specified. In Tidal hydrodynamics, ed.by B.B. Parker, John Wiley and Sons, Inc, pp 153-168.

[17] Bermudez A, Vazquez MA (1994) Upwind methods for hyperbolic conservation laws with source terms, Comput Fluids, 23(8):1049-1071.
[18] Zhou JG, Causon DM, Mingham CG, Ingram DM (2001) The surface gradient method for the treatment of source terms in the shallow-water equations, J Comput Phys, 168:1-25.
[19] Wu D, Fang G, Cui X, Teng F (2018) An analytical study of M_2 tidal waves in the Taiwan Strait using an extended Taylor method, Ocean Sci 14:117-126.